

ABSTRACT

Title of Document: ACCELERATED SELF-ASSEMBLY OF PEPTIDE-BASED NANOFIBERS USING NANOMECHANICAL STIMULUS

Jonathan P. Chang, Master of Science, 2010

Directed By: Assistant Professor/Advisor, Joonil Seog,
Department of Materials Science and
Engineering

One-dimensional nanostructures are ideal building blocks for functional nanoscale assembly. Peptide-based nanofibers have great potential for building smart hierarchical structures due to their tunable structures at a single residue level and their ability to reconfigure themselves in response to environmental stimuli. In this study, it was observed that a pre-adsorbed silk-elastin-based protein polymer self-assembled into nanofibers through a conformational change on the mica substrate. Furthermore, using atomic force microscopy, it was shown that the rate of the self-assembling process was significantly enhanced by applying a nanomechanical stimulus. The orientation of the newly grown nanofiber was mostly perpendicular to the scanning direction, implying that the new nanofiber assembly was locally activated with a directional control. The method developed as a part of this study provides a novel way to prepare a nanofiber patterned substrate using a bottom-up approach.

ACCELERATED SELF-ASSEMBLY OF PEPTIDE-BASED NANOFIBERS
USING NANOMECHANICAL STIMULUS

By

Jonathan P. Chang

Thesis submitted to the Faculty of the Graduate School of the
University of Maryland, College Park, in partial fulfillment
of the requirements for the degree of
Master of Science
2010

Advisory Committee:
Assistant Professor Joonil Seog, Chair
Professor Robert M. Briber
Professor Manfred Wuttig
Assistant Professor Santiago Solares

© Copyright by
Jonathan P. Chang
2010

Acknowledgments

I owe my deepest gratitude and appreciation to many people who made this study and Master's thesis possible. I would like to express my gratitude to Joonil Seog (my main advisor) for his dedication, valuable instruction and discussions throughout this project. I would also like to acknowledge Hamidreza Ghandehari, who generously provided silk-elastin-like polymer samples. Special thanks go to Karam Hiji and Zach Russ, who instructed me in atomic force microscope (AFM) operation and sample preparation. Thanks are also due to Santiago Solares, who developed the AFM simulation code, provided invaluable assistance with all aspects of software applications and engaged me in many great discussions. Jed Tan, Silvia Hoji Kang and Nitinun Varongchayakul also deserve my sincere appreciation for assistance in sample preparation and data analyses. Most importantly, I would like to thank my parents, Hsin-Li Chang and Yung-Shua Chiao, who selflessly and lovingly supported me and encouraged me to complete this study. Last, but not least, I would like to thank Jean Yang and David Gaddes for revising the thesis.

Table of Contents

Acknowledgments.....	ii
Table of Contents.....	iii
List of Tables.....	iv
List of Figures.....	v
List of Abbreviations and Acronyms.....	vi
Chapter 1: Introduction.....	1
1.1 Background: One-dimensional self-assembly.....	1
1.2 Silk-elastin-like protein polymer (SELP).....	2
1.3 Atomic force microscopy (AFM).....	5
Chapter 2: The effect of nanomechanical force on nanofiber self-assembly.....	8
2.1 Introduction.....	8
2.2 Methods.....	8
2.2.1 Experiments.....	8
2.2.1.1 Preparation of the SELP-815K sample.....	8
2.2.1.2 Nanomechanical force stimulus by AFM.....	10
2.2.2 Data Analysis.....	10
2.2.2.1 Quantification of fiber coverage.....	10
2.2.2.2 Quantification of fiber orientation.....	10
2.2.3 Simulation of the nanomechanical tapping force.....	11
2.2.3.1 Theoretical background.....	11
2.2.3.2 Tapping force simulation in different force levels.....	17
2.3 Results.....	18
2.3.1 The effect of the nanomechanical stimulus on nanofiber growth.....	18
2.3.2 The effect of the nanomechanical stimulus on nanofiber orientation.....	24
2.3.3 The quantification of nanomechanical stimulus using the simulation method.....	26
2.4 Discussion.....	28
Chapter 3: Heating effect on growth kinetics of nanofibers.....	29
3.1 Introduction.....	29
3.2 Methods.....	29
3.2.1 Experimental arrangement.....	29
3.2.1.1 SELP-815K sample preparation on the BioHeater™ heating chamber.....	29
3.2.1.2 SELP-815K AFM imaging in the BioHeater™ heating chamber.....	30
3.2.2 Data Analysis.....	30
3.3 Results.....	31
Chapter 4: Discussion.....	35
Chapter 5: Conclusions.....	40
Appendix I: NanoDrop™ operational procedures.....	41
Appendix II: Quantification of fiber coverage.....	42
Appendix III: Quantification of fiber orientation.....	43
Glossary of Symbols.....	44
Bibliography.....	46

List of Tables

Table 1. The parameters used in the AFM tapping force simulation.....	16
Table 2. The mean amplitude from the photodiode detector.	27
Table 3. The force and pressure calculated using a simulation method.....	28
Table 4. Activation energy on elongation and nucleation for various materials.....	39

List of Figures

Figure 1. The procedure of SELP protein polymer synthesis (The figure was modified from the original image in Megeed et al. [14] with permission).....	3
Figure 2. The complete amino acid residue sequence of SELP-815K. A schematic of the interchain hydrogen-bonded structure through silk blocks.....	4
Figure 3. A schematic illustration of AFM operation.....	6
Figure 4. A schematic illustration of the tapping mode AFM operating principle.....	7
Figure 5. Sample preparation procedures for SELP-815K for AFM imaging.....	9
Figure 6. A schematic illustration of the actual tip position under the base excitation system.	12
Figure 7. Contact force analysis during AFM tapping mode imaging.....	14
Figure 8. The AFM images ($2\ \mu\text{m} \times 2\ \mu\text{m}$) of SELP-815K nanofibers obtained in tapping mode at different time intervals. Arrows show new nucleation sites. The scale bars correspond to $1\ \mu\text{m}$	19
Figure 9. The AFM images ($1\ \mu\text{m} \times 1\ \mu\text{m}$) of SELP-815K adsorbed on mica surface and bare mica image.	20
Figure 10. The AFM images of SELP-815K nanofibers obtained in a tapping mode. (a) The first scanned image, (b) the second scanned image of the same area, (c) the zoomed-out image that includes the scanned area in (b). The scale bars correspond to $1\ \mu\text{m}$ and the red lines are pre-existing nanofibers in the figure (a).	22
Figure 11. (a) The nanofiber coverage as a function of time at different tapping pressures and (b) the final images after 25 minutes at each pressure level.	23
Figure 12. (a) The histogram of nanofiber orientation distributions with and without mechanical stimulus. (b) $50\ \text{nm} \times 50\ \text{nm}$ square area (blue box) was nanomechanically stimulated 512 lines and then zoomed out to $3\ \mu\text{m} \times 3\ \mu\text{m}$; (c) $50\ \text{nm} \times 3000\ \text{nm}$, 256 line rectangular stimulus (blue box) then zoomed out to $3\ \mu\text{m} \times 3\ \mu\text{m}$; and (d) $100\ \text{nm} \times 3000\ \text{nm}$, 512 line rectangular stimulus (blue box) then zoomed out to $3\ \mu\text{m} \times 3\ \mu\text{m}$. The scale bars correspond to $1\ \mu\text{m}$	25
Figure 13. The histogram of amplitude distributions at various combinations of set-point and free amplitude.	26
Figure 14. The example of tip trajectory at set-point amplitude: free amplitude = 760 mV; 800 mV.	27
Figure 15. The temperature variation profile during the experiment.....	31
Figure 16. The SELP-815K AFM images under different temperatures. The scale bars correspond to $1\ \mu\text{m}$	32
Figure 17. The length of nanofibers measured at different temperatures.	33
Figure 18. The Arrhenius plot of elongation rates as a function of inverse temperature.	34
Figure 19. The nanofiber coverage as a function of tapping pressures at different time periods.....	36
Figure 20. A schematic illustration of fiber growth orientation.	37
Figure A1. An example of measurement of nanofiber orientation.	43

List of Abbreviations and Acronyms

SELP	silk-elastin-like protein
PCR	polymerase chain reaction
AFM	atomic force microscopy
TM-AFM	tapping mode atomic force microscopy
PD	photodetector
PSD	power spectral density

Chapter 1: Introduction

The goal of this work was to study the fundamental mechanism of surface-facilitated self-assembly and to develop a method to control self-assembly processes by environmental changes. Previous studies found that the self-assembly of silk-elastin protein polymer on a mica surface was significantly dependent on the surface properties and ionic strength; however, the mechanical effect on the surface has not been demonstrated. In this study, a successful technique was developed to activate the self-assembly locally with directional control. This technique may be applicable in preparing one-dimensional patterned surfaces using peptide-based polymeric materials.

1.1 Background: One-dimensional self-assembly

One-dimensional nanostructures are ideal building blocks for functional nanoscale assembly due to their capacity for electrical and thermal transportation, as well as having mechanical properties that allow for interconnections into a functional unit. Numerous research teams are focusing on controlling the self-assembly process to develop a nanostructure with periodic patterns [1-3]. The solid-state materials behave differently in a one-dimensional scale; for example, carbon nanotube was found to have semiconductor properties and it was used as a transistor [4]. Furthermore, chemically modified silicon nanowire can sense the pH on the single molecular level [5]. However, solid-state material is difficult to manipulate *in situ*. Once the structure has formed, it is hard to modify the structure to tailor its size and orientation.

In nature, spontaneous organization often occurs in a hierarchical manner in a wide range of lengths, creating a higher-order structure built from a pre-assembled structure in a stepwise fashion [2, 6-7]. During this process, the preformed substrate can often provide crucial cues in facilitating a subsequent assembly step [8]. Local geometric constraints and mostly non-covalent interactions--such as hydrogen bonding, or hydrophobic or electrostatic interactions--are driving forces for self-assembled structures [9]. The formation of one-dimensional self-assembled peptide nanostructures on the substrate has been reported [8, 10]. These peptide-based one-dimensional nanostructures have great application in a biosensor [11] and as a nanopatterned substrate for cell migration studies [12]. However, in these cases, controlling location and direction of the nanostructures on the substrate to create a well-defined one-dimensional nanoscale pattern has been quite challenging.

1.2 Silk-elastin-like protein polymer (SELP)

The silk-elastin-like protein (SELP) polymer is a genetically engineered protein block copolymer [13] made of silk-like blocks (Gly-Ala-Gly-Ala-Gly-Ser) from *Bombyx mori* (the silkworm) and elastin-like blocks (Gly-Val-Gly-Val-Pro) from mammalian elastin [14]. Silk is a well known natural crystalline protein that can produce high tensile strength for textile manufacturing [15]. Its distinctive mechanical properties and biocompatibility have recently spurred interest in incorporating reprocessed silks into biotechnological materials and biomedical applications [16-17]. Elastin is a connective tissue protein that has high elasticity, large strains and low stiffness; it is one of the rubber-like proteins that function in the storage of elastic strain energy [18]. It is also flexible, extends beyond 100%, and has a very low

modulus of elasticity (~0.001 GPa). SELP polymers combine the repeating blocks of amino acids that are responsible for the strength of silk and the elasticity of elastin. The structure of SELPs can be controlled at the single amino acid residue level, which allows strategic introduction of various motifs responsible for self-assembly, stimuli-sensitivity, biorecognition and biodegradation.

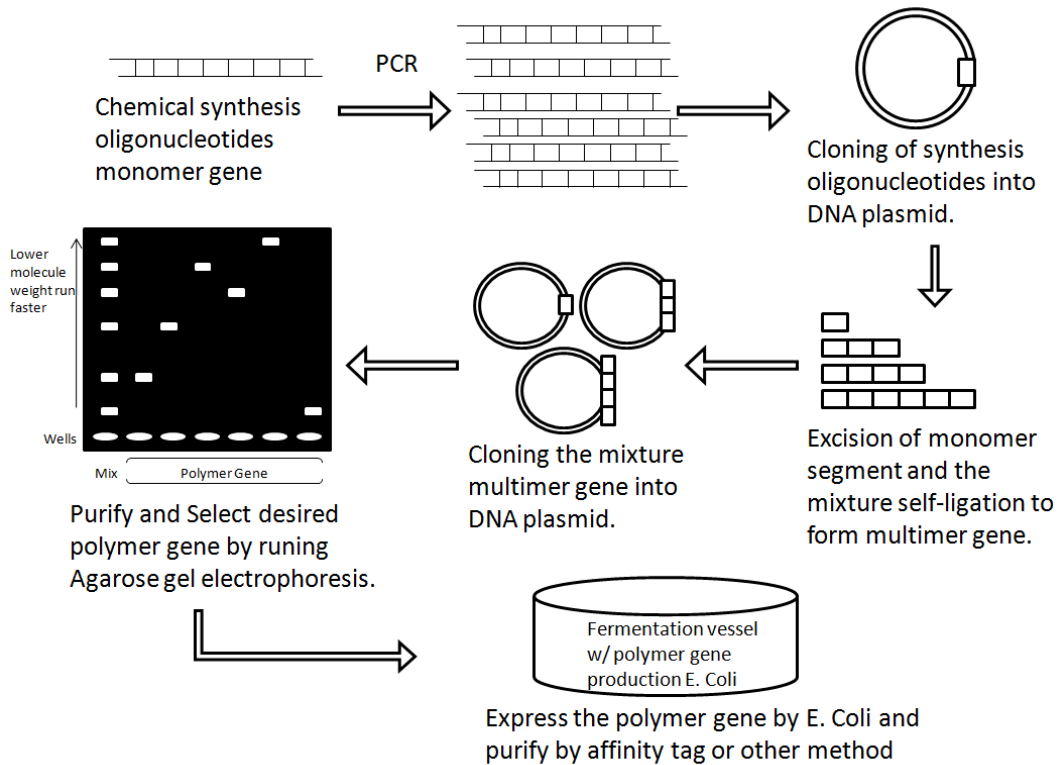


Figure 1. The procedure of SELP protein polymer synthesis (The figure was modified from the original image in Megeed et al. [14] with permission).

The synthetic methods for SELPs production were first developed by Ferrari et al. [16, 19] The process can be broadly separated into three steps (see Figure 1). First, a suitable monomer gene sequence is designed by chemical synthesis, polymerase chain reaction (PCR) and annealing of oligonucleotides. Next, the oligonucleotides are inserted into a DNA plasmid, followed by transfer to PCR or

The structure of SELPs can be controlled at the single amino acid residue level, allowing for the strategic introduction of various functional motifs for hierarchical self-assembly, stimuli-sensitivity and biorecognition [14, 21]. At human body temperature, SELP forms a hydrogel that can be used in injectable biomaterials for drug delivery [17, 22] and tissue engineering [23-24]. Recently, our group observed that SELPs self-assembled into a nanofiber structure on a specific substrate; growth kinetics were inhibited by increasing salt concentration [25].

1.3 Atomic force microscopy (AFM)

AFM has been widely used in many scientific research fields to investigate surface properties. As a branch of scanning probe microscopy, which measures the local interaction between the surface and a small probe, AFM can investigate, not only surface topography, but also electronic structure and electric and magnetic fields. In contrast to transmission electron microscopy (TEM) and scanning electron microscopy (SEM), AFM also provides some information about biological tissues and large organic molecules without damaging the samples via electron charge and high vacuum environments. Moreover, AFM can be operated under aqueous conditions, which enables many biological samples to retain their structure and function.

The AFM has a cantilever with a sharp tip at its end, which can be used to scan through sample surfaces (Figure 3). The sample is placed on the scanner, whereas the cantilever and tip are positioned close to the surface using a macroscopic positioning device. As the laser beam reflects off the top of the tip, the position and

intensity of the reflected beam are detected by a photodiode that determines the deflection of the cantilever. A feedback loop system receives the signal from the photodiode and controls the tip oscillation and position depending on the operating mode.

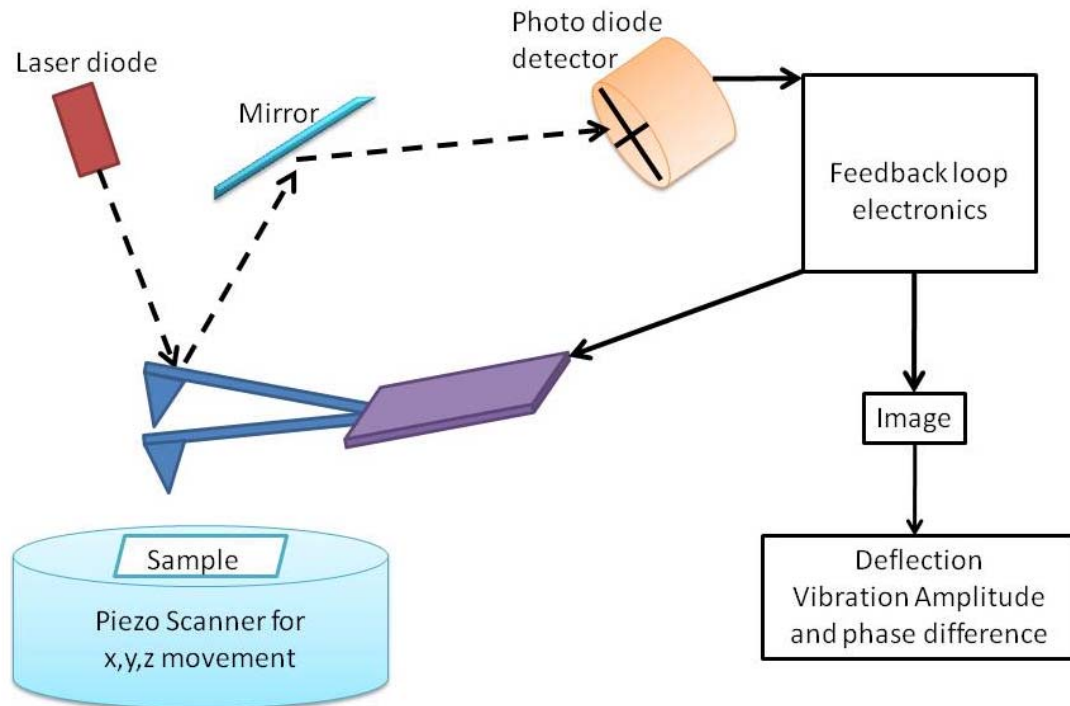


Figure 3. A schematic illustration of AFM operation.

AFM resolution mainly depends on the radius of curvature of the tip. An ideal AFM instrument is free of thermal, electronic and vibrational noise and its resolution is limited only by laser shot noise. In ultra-high vacuum conditions and low temperatures, the AFM technique can provide a true atomic resolution. Unfortunately, the tip-surface interactions significantly decrease the resolution, especially in aqueous imaging, not only because of the noise sources described above, but also from hydrodynamic forces.

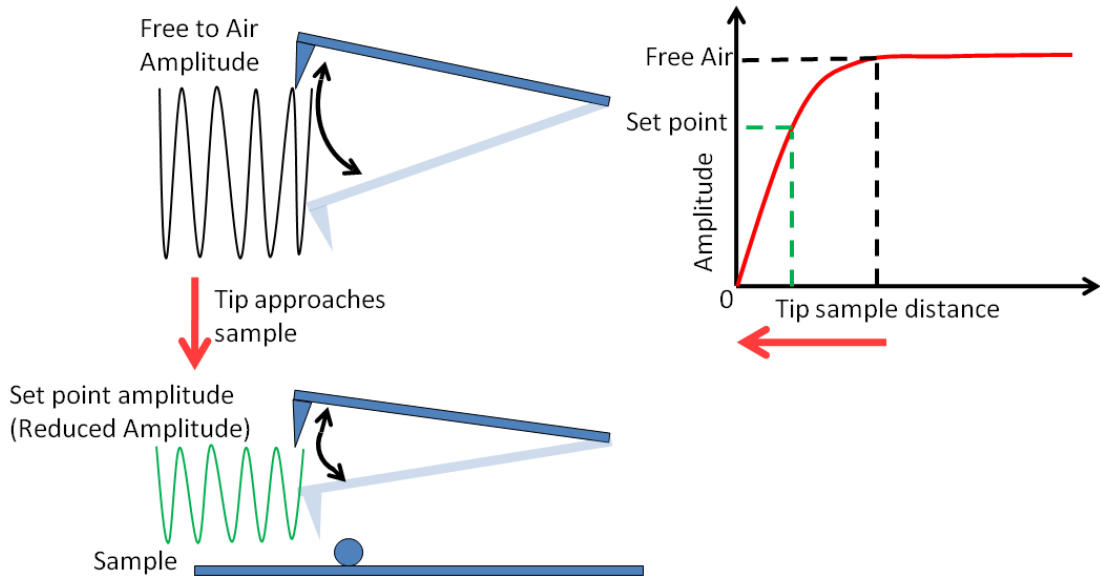


Figure 4. A schematic illustration of the tapping mode AFM operating principle.

Thus, when operating tapping mode (amplitude modulation [26]) AFM (TM-AFM) in a fluid medium, the ratio of the set-point amplitude to free to air oscillation amplitude (here, referred to as target amplitude) will be increased to the maximum, to minimize the potential sample damage, without compromising the stable imaging and high resolution (Figure 4). By changing the free to air oscillation amplitude and set-point amplitude combination, the tapping force level applied on the surface can be adjusted, as required.

Chapter 2: The effect of nanomechanical force on nanofiber self-assembly

2.1 Introduction

Unlike SELP 415K and 47K, SELP 815K has four more silk blocks in its repeating units and tends to form long nanofibers. Previous studies revealed that SELP 415K and 47K tend to form short and straight nanofibers only on the surface and that the growth rate is dependent on environmental conditions, such as salt concentration, pH and surface properties [25]. The nanofiber density of SELP 815K is much lower than in SELP 415K and 47K. However, despite the morphological differences, the SELP 815K nanofiber has similar height (~3.9 nm) and width (~23.4 nm) as SELP 415K and 47K. Here, we investigated the mechanism of the surface-facilitated self-assembly and the effect of mechanical force on nanofiber growth.

2.2 Methods

2.2.1 Experiments

2.2.1.1 Preparation of the SELP-815K sample

We began with frozen SELP-815K solution (500 μ l 12% in phosphate buffered saline [PBS] solution) provided by Dr. Hamidreza Ghandehari, Univ. Utah. Next, 100 μ l of the solution was diluted with PBS in a 1:10 ratio. The diluted solution was subsequently separated into 10 tubes and frozen for later use. To prepare SELP solution, the frozen 1.2 % SELP-815K stock solution was thawed at 4 °C, followed by

centrifugation at 9000 rpm for three minutes to remove the aggregated protein polymers.

The concentration of the extracted clear solution was measured by NanoDrop (Thermo Fisher Scientific, Inc., Wilmington, DE). The sample was then diluted with distilled water to prepare polymer concentrations of 5 $\mu\text{g}/\text{ml}$.

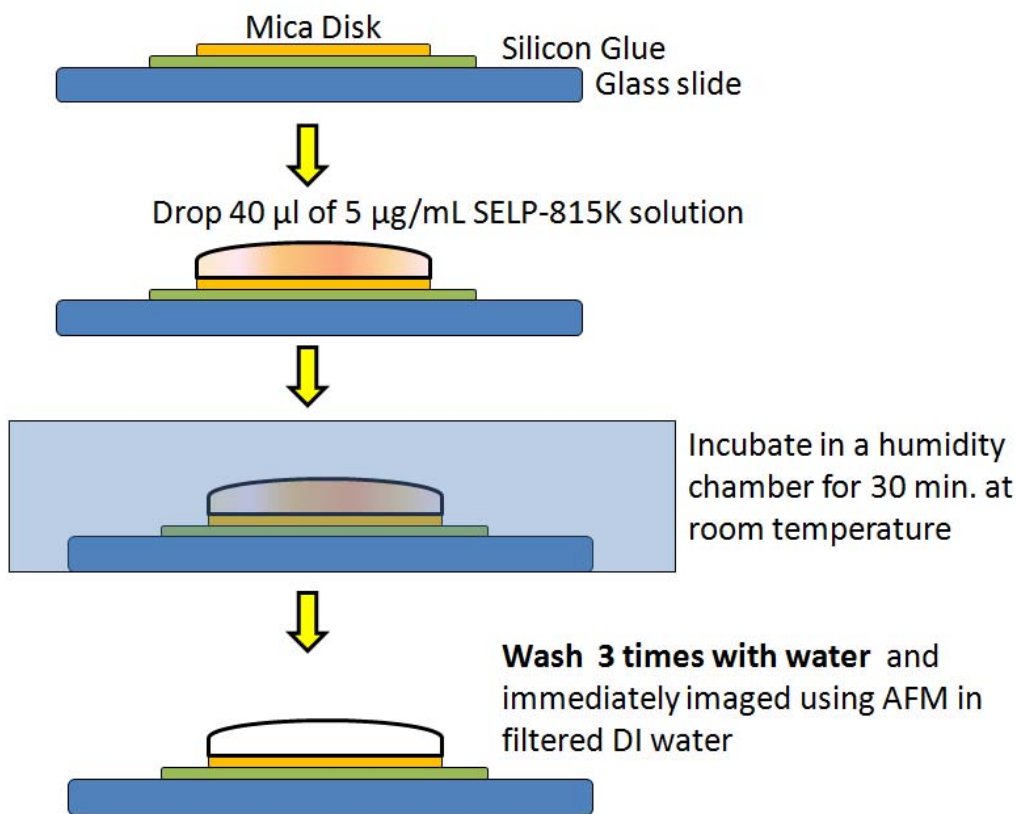


Figure 5. Sample preparation procedures for SELP-815K for AFM imaging.

To prepare the samples for AFM imaging (Figure 5), 40 μL of each SELP solution was dispensed on a freshly cleaved 8 mm \times 8 mm mica surface (Ted Pella, Inc., Redding, CA). The samples were incubated for 30 minutes in a humidity chamber at room temperature, and then washed three times with distilled water.

2.2.1.2 Nanomechanical force stimulus by AFM

AFM imaging was performed using a Molecular Force Probe-3D instrument (MFP-3D™, Asylum Research Inc., Santa Barbara, CA) in filtered distilled water at room temperature. An MLCT probe (Brucker Corp., Camarillo, CA) with a spring constant ranging from 0.03 to 0.06 N/m was used for imaging, as the higher free amplitude and the lower set-point amplitude yield greater tapping force on the protein. Three different force levels were selected to obtain the data set. Once the results produced by each force level were obtained, a computer simulation was performed to calculate the actual force and then identify a correct amplitude combination for implementation in the instrument to be used in experiments.

2.2.2 Data Analysis

2.2.2.1 Quantification of fiber coverage

The ImageJ program (<http://rsbweb.nih.gov/>) was used to measure the fiber coverage of the mica surface. The AFM MFP-3D™ instrument has built-in analysis software Igor Pro™ (WaveMetrics Inc., Portland, OR) that calculates thresholds using the WaveMetrics Image Threshold function. We chose a threshold (cut-off value) so that the width of the nanofiber is ~ 20 nm, which is the same as the actual width of the nanofiber. The threshold was adjusted to provide an ~20 nm nanofiber width throughout the comprehensive image analysis. The surface coverage was measured by using ImageJ to count the pixels occupied on the measured area.

2.2.2.2 Quantification of fiber orientation

Since the nanofibers in the AFM images demonstrated a directional growth pattern, the ImageJ software was used to analyze nanofiber orientation in a

quantitative manner. We used the ImageJ plug-in, OrientationJ, to carefully draw the outline of each fiber and measure the asphericity of the outline, then fit it within an ellipse. The semi-major axes of those ellipses can represent the fibers' orientation. The protocol for measuring nanofiber orientation was developed by Sylvia Kang, a summer high school student, and it is attached as Appendix III.

While the data range from +90 to -90 degrees, only the angle between the horizontal scanning direction and the fiber needs to be considered, as the negative values are identical to the corresponding positive values. Thus, the data can be plotted on a bar chart in a range of 15 degrees.

2.2.3 Simulation of the nanomechanical tapping force

In TM-AFM, the tapping force is produced momentarily from tip impact to the surface, which produces a force. By controlling the set-point amplitude and free amplitude combination, the force level that taps on the surface can be adjusted.

2.2.3.1 Theoretical background

In this study, the base (cantilever holder) excitation system was used to retrieve an image of surface topology. In the base excitation system, a cantilever holder is driven at its resonance frequency by a piezoactuator that is in contact with the holder. The base oscillation causes additional displacement of the cantilever holder so that the actual position is the sum of the deflection of the cantilever and the displacement of the cantilever holder (Figure 6) [27].

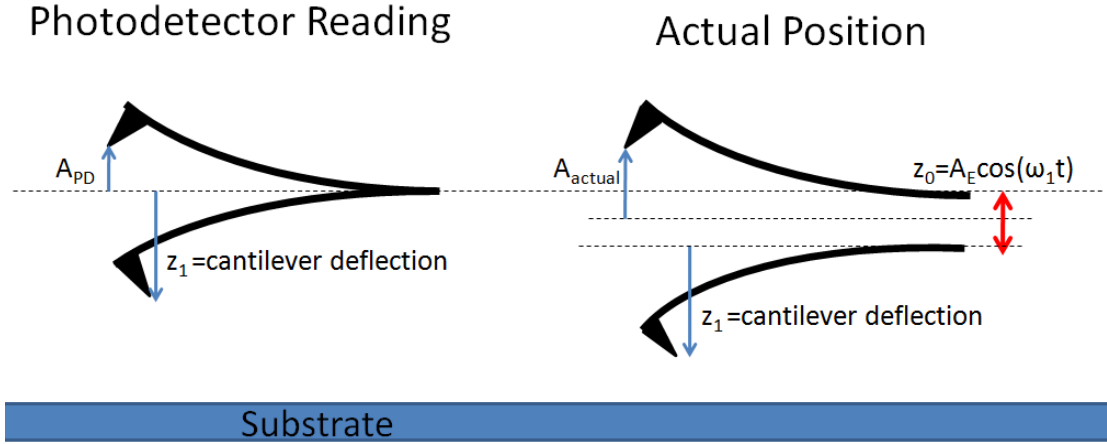


Figure 6. A schematic illustration of the actual tip position under the base excitation system.

A_E is the excitation amplitude (here, referred to as drive amplitude), ω_1 is the first eigenmode resonance frequency, z_0 is the position of the piezo actuator and z_1 is the cantilever deflection, which is the photodetector reading we read from the experimental instrument. Using the deflection value, we can convert it to actual amplitude (A_{actual}). The actual amplitude usually is larger than the photodetector amplitude (A_{PD}). Thus, the actual tip position (u) is the sum of the piezo location and the first and second eigenmode cantilever deflections, as given by the expression below:

$$u = z_0 + z_1 + z_2$$

with,

$$z_0(t) = A_E \cos(\omega_1 t),$$

where z_2 is the deflection from the second eigenmode. The second cantilever eigenmode can be temporarily excited in liquid environments, changing the tip-sample force trajectory significantly, and creating multiple tip-sample impacts for each oscillation of the fundamental eigenmode [28-30]. To quantify the tapping force

exerted on the surface, the tapping mode process was simulated using a two-eigenmode cantilever model with the customary sinusoidal excitation of the fundamental eigenmode [28-29, 31]. The tapping force for each eigenmode is written by the expression below:

Eigenmode Mode 1:

$$F_1(t) = m_{eff} \frac{d^2 z_1}{dt^2} = -k_1(z_1 - z_0(t)) - \frac{m_{eff} \omega_1}{Q_1} \frac{dz_1}{dt} + F_{T-S}(z)$$

Eigenmode Mode 2:

$$F_2(t) = m_{eff} \frac{d^2 z_2}{dt^2} = -k_2(z_2 - z_0(t)) - \frac{m_{eff} \omega_2}{Q_2} \frac{dz_2}{dt} + F_{T-S}(z)$$

with

$$m_{eff} = \frac{k}{\omega_1^2},$$

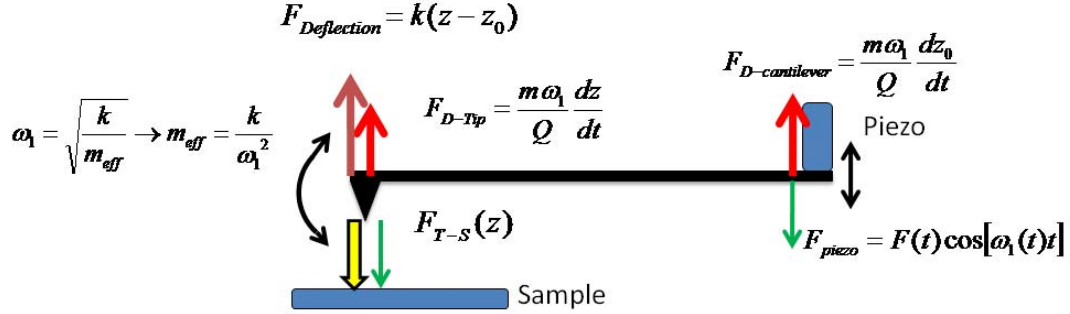
where m_{eff} is the effective mass of the tip, k_1 and k_2 are the spring constants, ω_1 and ω_2 are the oscillation frequencies, and Q_1 and Q_2 are quality factors of each eigenmode from experimental data. The quality factor is defined as

$$Q \equiv \frac{\omega_1 m}{b},$$

where b is the damping factor of damped simple harmonic motion.

In TM-AFM, the system actively controls the feedback loop within a proportional-integral control through the tip oscillation amplitude or the photodetector amplitude as the feedback parameter. Furthermore, the amplitude controller in the experimental system should take the non-zero response time (20 sec)

into account. The force equilibrium diagram is given below (Figure 7) to analyze the first eigenmode tapping force on the sample.



Instantaneous sum of forces

$$m_{eff} \frac{d^2 z}{dt^2} = -k(z - z_{eq}) - \frac{m_{eff} \omega_1}{Q} \frac{dz}{dt} - \frac{m \omega_1}{Q} \frac{dz_0}{dt} + F_{T-S}(z) + F(t) \cos[\omega_1(t)t]$$

Figure 7. Contact force analysis during AFM tapping mode imaging.

According to the force analysis, taking the second eigenmode into account, the instantaneous sum of forces acting on the tip can be written by the expression below:

$$m_{eff} \frac{d^2 z}{dt^2} = -k(z_1 + z_2 - z_0(t)) - m_{eff} \left(\frac{\omega_1}{Q_1} + \frac{\omega_2}{Q_2} \right) \frac{dz}{dt} - \frac{m \omega_1}{Q_1} \frac{dz_0}{dt} + F_{T-S}(z) + F(t) \cos[\omega_1(t)t]$$

where m_{eff} is the effective mass of the tip, k is the spring constants, ω_1 is the oscillation frequency, and Q_1 and Q_2 are quality factors of each eigenmode from experimental data. $F_{Deflection}$ is the force applied by the cantilever deflection, $F_{D-cantilever}$ and F_{D-Tip} is the damping force from the liquid damping on the cantilever and tip, respectively (Figure 7). In addition, repulsive tip-sample interactions ($F_{T-S}(z)$) were introduced through the Derjaguin-Müller-Toporov (DMT) model:

$$F_{T-S}(z) = \frac{4}{3\pi\kappa_{eff}} \sqrt{R}(a_{DMT} - z)^{3/2} - \frac{HR_{tip}}{6a_{DMT}^2} \text{ for } z \leq a_{DMT}$$

with

$$\kappa_{eff} = \frac{1 - \nu_{tip}^2}{\pi E_{tip}} + \frac{1 - \nu_{sample}^2}{\pi E_{sample}},$$

where H is the Hamaker constant, R_{tip} is the tip radius, a_{DMT} is the interatomic distance parameter of a Derjaguin–Müller–Toporov (DMT) potential, and E_{tip} , ν_{tip} and E_{sample} , ν_{sample} are, respectively, the Young's modulus and Poisson coefficient of the tip and the sample.

To calculate a range for the maximum tapping force, the simulations considered the control capability, quantified through the standard deviation of the experimental amplitude error (~ 0.1 nm) for the entire scan.

Parameters for tip and sample elasticity were selected based upon the tip geometry and tip material used in the measurements (Table 1). Attractive interactions were ignored, since they are significantly reduced in liquid environments.

Table 1. The parameters used in the AFM tapping force simulation.

Fundamental cantilever eigenfrequency	14.5 kHz
Second cantilever eigenfrequency	90.625 kHz
Cantilever excitation frequency	14.5 kHz
Fundamental eigenmode force constant	0.003 N/m
Second eigenmode force constant	0.1172 N/m
Fundamental eigenmode quality factor	2
Second eigenmode quality factor	6
Cantilever base excitation amplitude	(give the appropriate range used) nm
Cantilever amplitude set point	(give the appropriate range used) nm
Tip and sample Poisson ratio	0.3
Tip modulus of elasticity	130 GPa
Sample modulus of elasticity	2 GPa
Tip radius	5 nm
Oscillation equilibration time	300 fundamental periods (~0.021 ns)

Finally, all the equations were written in the C code and an executable file was created, an appropriate range was supplied to the input file and the simulation was run. To convert the force level to pressure level, the average amplitude was retrieved and that value minus three standard deviations from the mean was used. The

calculated force level was normalized by the nominal radius of the AFM tip to obtain an approximate pressure at each condition.

2.2.3.2 Tapping force simulation in different force levels

As per the discussion above, the excitation amplitude and amplitude read from the instrument (A_{PD}) was not the true amplitude (A_{actual}). The excitation amplitude (A_E) was measured, yielding the same photodetector amplitude as the instrument reading. The procedure for obtaining the actual excitation amplitude and true amplitude is described below.

First, to find the actual excitation amplitude (A_E), the amplitude set point was set to about 5% higher than twice the excitation amplitude (this ensures that the cantilever will never touch the sample, and the trajectory is double-checked to make sure that the oscillation, indeed, never reaches the surface) and the simulation is run. This will show the relationship between the true free amplitude and the photodetector (PD) free amplitude. Based on this value, the excitation is adjusted proportionally to get the same PD amplitude as the instrument's free amplitude reading.

The second step is finding the amplitude set point that will display a "PD amplitude" in the program equal to the experimental amplitude set point. This is done by setting the amplitude set point to below the actual free amplitude (that is, below twice the excitation amplitude) and repeatedly adjusting this set point until the "PD amplitude" gives the same value as the experimental amplitude set point (making sure that the amplitude set point in the input file is always lower than the actual free oscillation amplitude).

Once the above two steps have been completed, the experiment and the simulation will be in agreement, and the data for each force level can be collected. It is necessary to use the recorded amplitude mapping to plot the amplitude distribution histogram and fit Gaussian function to it and retrieve the mean and standard deviation. Because the lower amplitude produced a larger force, use the minus three times standard deviation to find the upper force range and repeat it in different amplitude combinations.

2.3 Results

2.3.1 The effect of the nanomechanical stimulus on nanofiber growth

The AFM images of the same area, taken at different time intervals, illustrate that SELP-815K formed nuclei at various locations and slowly self-assembled to form a nanofibrous structure (Figure 8). This is quite surprising, since the sample was washed thoroughly with water after incubation, implying that there should be no supply of protein from the bulk phase for further growth. This observation strongly suggests that nucleus formation and nanofiber self-assembly occurred through conformational changes of the pre-adsorbed SELP-815K on the mica surface.

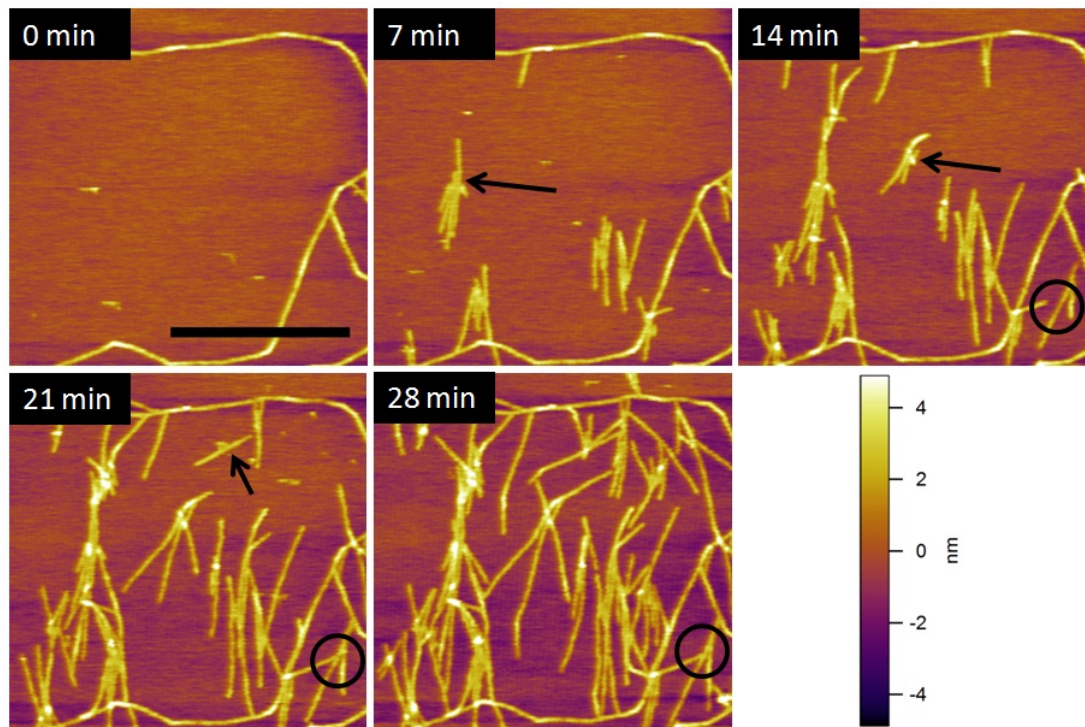


Figure 8. The AFM images ($2\ \mu\text{m} \times 2\ \mu\text{m}$) of SELP-815K nanofibers obtained in tapping mode at different time intervals. Arrows show new nucleation sites. The scale bars correspond to $1\ \mu\text{m}$

After a 30-min incubation and washing, nanofibers are usually sparsely formed throughout the mica surface, but the area imaged at 0 min was chosen so that there would be few observed nucleation sites. The images taken after 7 min show that new nucleation sites formed on the mica and grew into nanofibrous structures at random locations. A nucleation site is identified with an arrow in the images to follow the formation of the nanofibers at this site. Not only were new nanofibers formed from the new nucleation sites, but the existing fibers also kept growing, as evidenced in the 14-min and 21-min images. In the 14-min image, the preformed nanofiber in the circle was growing continuously. In the 28-min image, the circle shows the junction formed by physically blocking one end of the growing nanofiber. This type of junction is observed at many different locations, indicating the important role of

the surface on the self-assembly process. The high-resolution AFM image revealed the presence of the pre-adsorbed SELP-815K layer on the mica surface (Figure 9). The pre-adsorbed layer seems to form a monolayer composed of globular-shaped protein molecules.

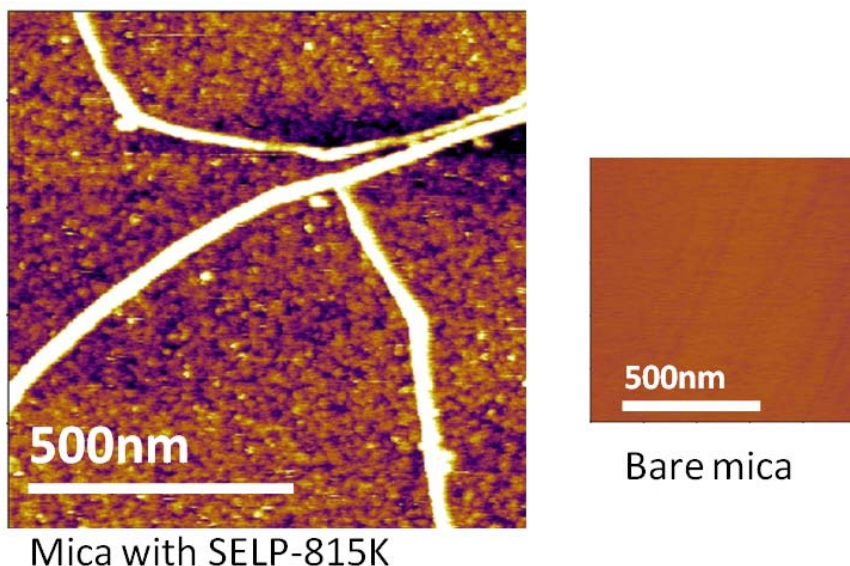


Figure 9. The AFM images ($1 \mu\text{m} \times 1 \mu\text{m}$) of SELP-815K adsorbed on mica surface and bare mica image.

The presence of densely packed globular proteins on the surface confirms that the new nanofiber formation originates from conformational changes of pre-adsorbed protein. In other areas with some preformed nanofibers, we observed a dramatic effect of the AFM tapping mode imaging on the nanofiber assembly. Figure 10a is the first scanned image using AFM, which shows some nanofibers formed during incubation. When the same area was scanned a second time, the density of nanofibers was significantly increased (Figure 10b). The red lines in Figure 10b represent the nanofibers imaged in the first scan. The drastic effect of the AFM scan on nanofiber growth is clearly visible in the zoomed-out image in Figure 10c, where the sharp contrast in nanofiber density was clearly observed between the area scanned once

(outside the square) and the area scanned twice (inside the square). This remarkable difference clearly indicated the strong effect of the AFM tapping force on the self-assembly of nanofibers.

To further investigate this novel effect of nanomechanical stimulus on self-assembly, the ratio of the amplitude set point and the free amplitude in tapping mode were varied. In tapping mode imaging, the AFM tip briefly contacts the surface, exerting momentary impact [29, 32]. By varying the set-point amplitude at a fixed free amplitude, the tapping force level was adjusted systematically. To quantify the tapping force exerted on the surface, the tapping mode process was simulated using a two-eigenmode cantilever model. The calculated force level was normalized by the nominal radius of the AFM tip to obtain an approximate pressure at each condition. The coverage of nanofibers under calculated tapping pressures varied from 18.8 MPa to 213 MPa and was then measured at five different time points (Figure 11). Overall, coverage increased as a function of time under the range of pressures tested. The rate of percent coverage change was increased from ~ 0.2 %/min at 18.8 MPa to ~ 2 %/min at 213 MPa. This observation clearly indicates the effect of local nanomechanical pressure on enhancing the self-assembly of nanofibers.

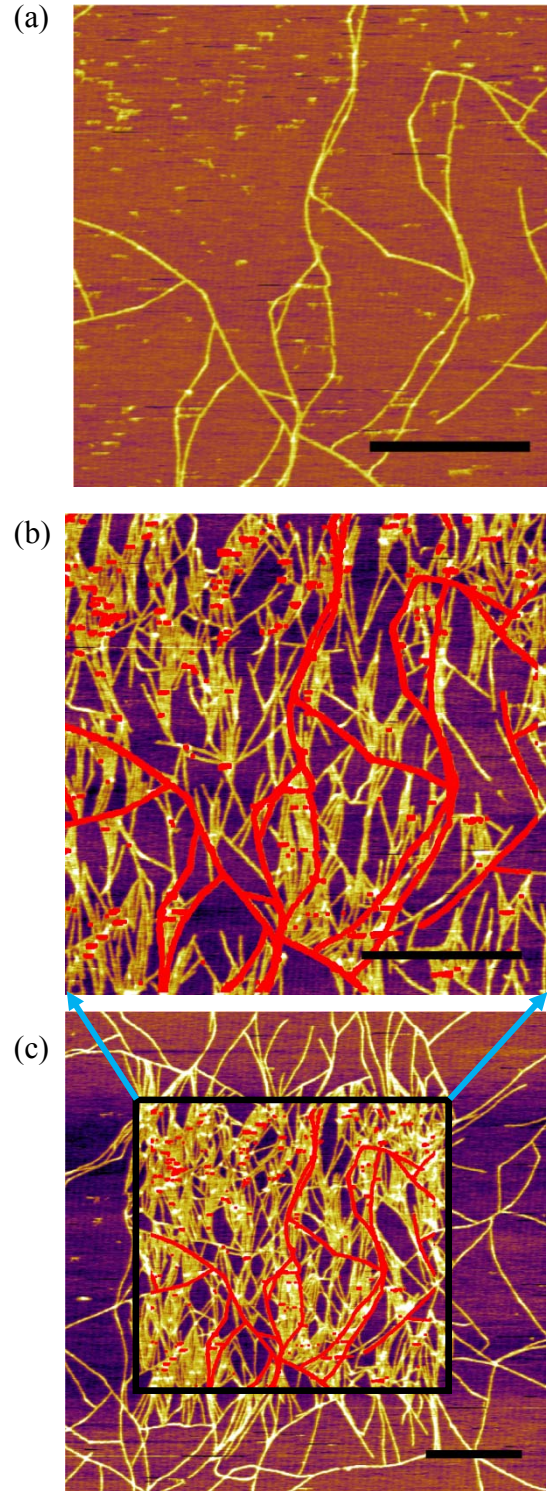


Figure 10. The AFM images of SELP-815K nanofibers obtained in a tapping mode. (a) The first scanned image, (b) the second scanned image of the same area, (c) the zoomed-out image that includes the scanned area in (b). The scale bars correspond to 1 μm and the red lines are pre-existing nanofibers in the figure (a).

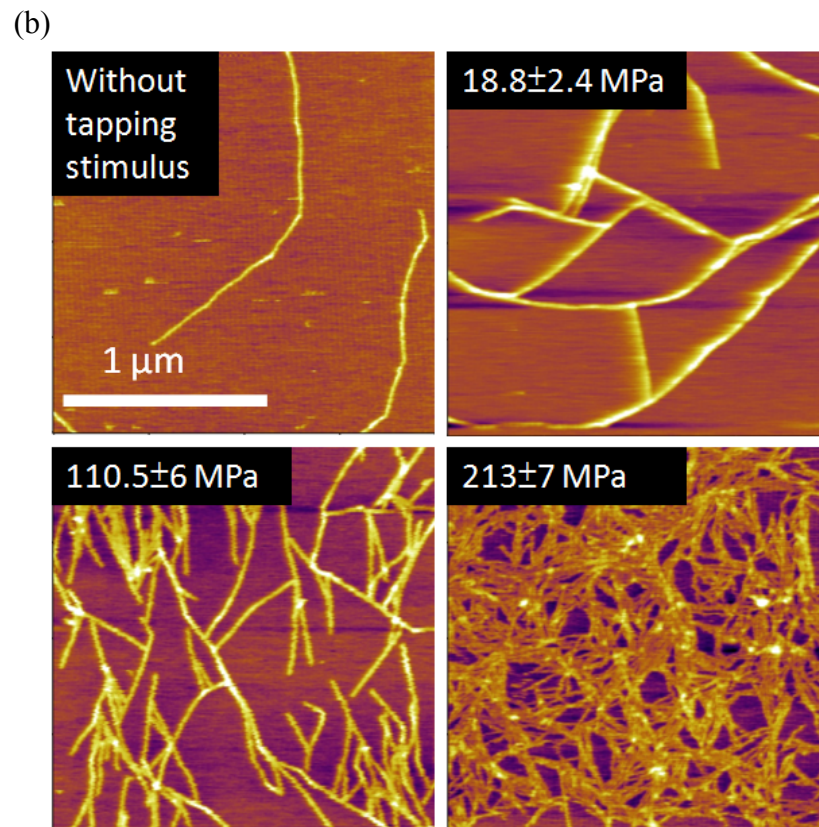
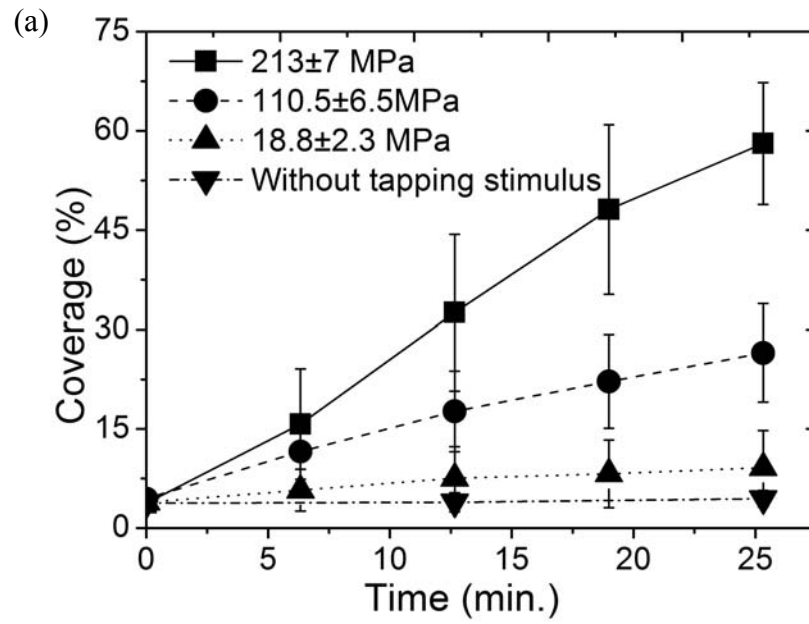


Figure 11. (a) The nanofiber coverage as a function of time at different tapping pressures and (b) the final images after 25 minutes at each pressure level.

2.3.2 The effect of the nanomechanical stimulus on nanofiber orientation

The newly grown nanofibers, under the influence of AFM scanning, seemed to have a strong preference in their growth direction. We used the ImageJ and OrientationJ plug-in to analyze the orientation of each nanofiber with respect to the AFM scanning direction (horizontal in the AFM images) (Figure 12). The orientation of the nanofibers formed during incubation (without any mechanical stimulus) was evenly distributed between 0° and 90° , indicating that the crystal plane of the mica had no effect on their growth direction. In sharp contrast, 80% of the newly grown fibers after nanomechanical stimulus by AFM showed a preferred orientation between 60° and 90° . This suggests preferential growth perpendicular to the AFM scanning direction, and confirms the effect of tapping mode imaging on self-assembly.

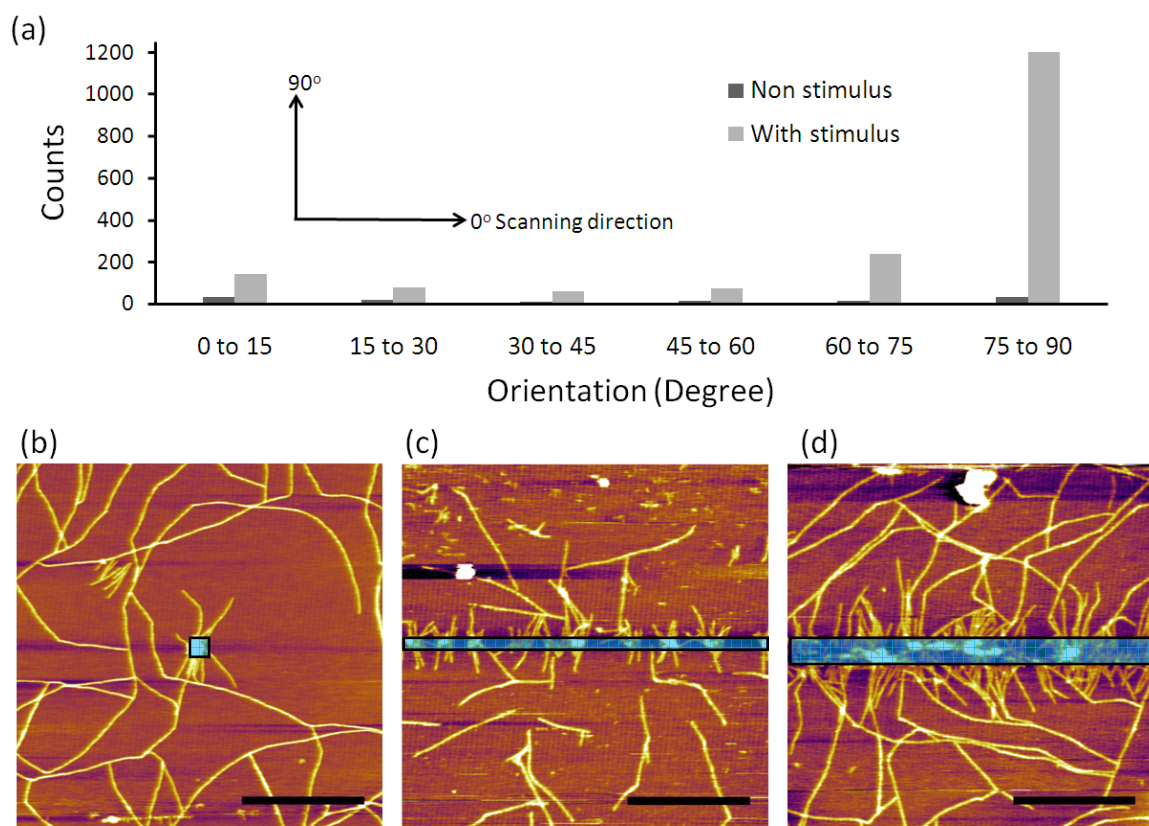


Figure 12. (a) The histogram of nanofiber orientation distributions with and without mechanical stimulus. (b) 50 nm × 50 nm square area (blue box) was nanomechanically stimulated 512 lines and then zoomed out to 3 μm × 3 μm; (c) 50 nm × 3000 nm, 256 line rectangular stimulus (blue box) then zoomed out to 3 μm × 3 μm; and (d) 100 nm × 3000 nm, 512 line rectangular stimulus (blue box) then zoomed out to 3 μm × 3 μm. The scale bars correspond to 1 μm.

Additionally, to control the peptide assembly and pattern of the nanofibers at a desired location on the surface, nanomechanical stimulus was applied to a small open area (Figure 12 b-d). The central 50 nm × 50 nm area was scanned and then zoomed out immediately, demonstrating that SELP-815K formed a nucleation site and that growth occurred outside of the original scanning area (Figure 12b). In Figures 12c and 12d, the rectangular areas, 50 nm × 3000 nm and 100 nm × 3000 nm, were tapped and then zoomed out, demonstrating a perpendicular fiber growth in the outer

area. This clearly indicates that the fiber growth can be initiated by the AFM tapping imaging process.

2.3.3 The quantification of nanomechanical stimulus using the simulation

method

To convert the force level to the pressure level, the average amplitude minus three standard deviations was retrieved. From the experimental amplitude data (Figure 13), Gaussian fitting was performed on the histogram to obtain the mean amplitude and standard deviation for each experiment. The results are listed in Table 2.

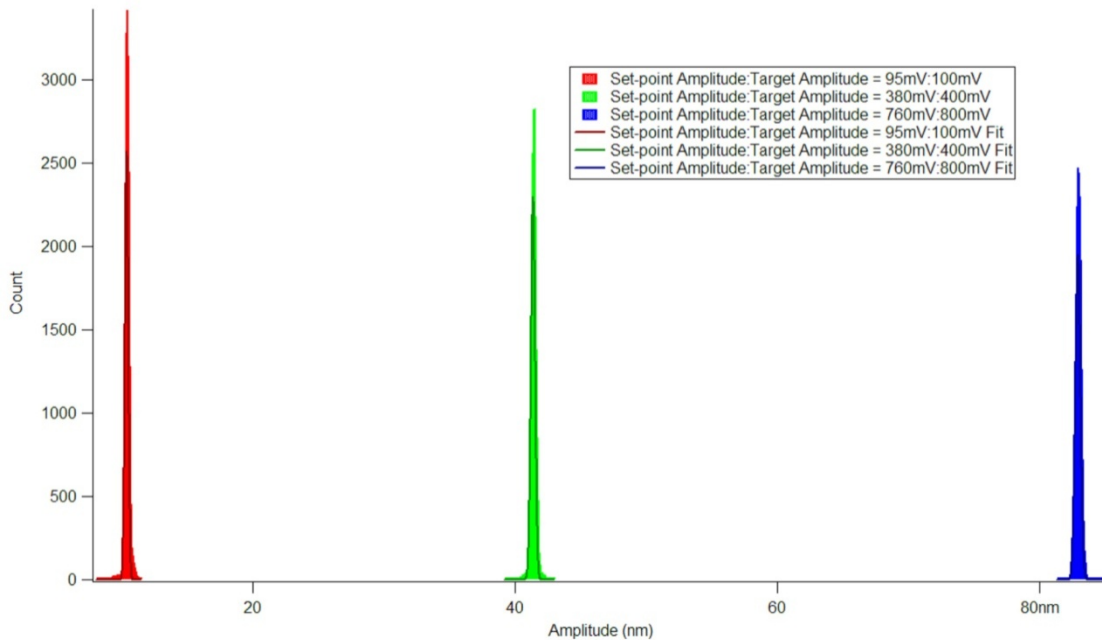


Figure 13. The histogram of amplitude distributions at various combinations of set-point and free amplitude.

Table 2. The mean amplitude from the photodiode detector.

Set-point amplitude: Free amplitude	Mean Amplitude (nm)	Standard Deviation (nm)
95mV : 100 mV	10.42	0.07
380 mV : 400 mV	41.37	0.07
760 mV : 800 mV	82.9	0.09

Once the amplitude range from the photodiode detector was obtained, the amplitude value minus 3σ was used to simulate AFM tapping force. The tip trajectory is plotted in Figure 14, which shows the surface was impacted by the tip exerting force on the substrate. The normalized pressure level at each condition is shown in Table 3.

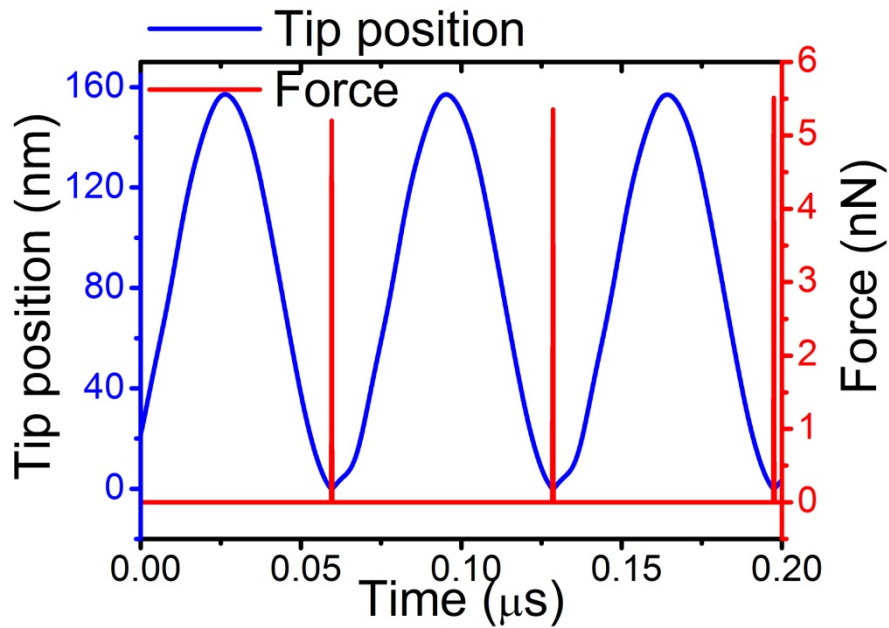


Figure 14. The example of tip trajectory at set-point amplitude: free amplitude = 760 mV: 800 mV.

Table 3. The force and pressure calculated using a simulation method.

Set-point amplitude: Free amplitude	Force level (nN)	Maximum force (nN)	Pressure level (MPa)	Maximum pressure (MPa)
95mV : 100 mV	0.4	0.5	16.4	21.1
380 mV : 400 mV	2.6	2.9	104	117
760 mV : 800 mV	5.2	5.5	206	220

2.4 Discussion

At present, there are no precise structural data for SELP-815K to confirm conformation on a mica surface. Thus, it is essential to gather further data from high-pressure X-ray diffraction and nuclear magnetic resonance (NMR) analysis of SELP-815K to confirm the structure. However, results of the experimental procedure described above allow the researcher to propose several hypotheses that could explain the fiber growth mechanism. The possible hypotheses will be discussed at the end of the document.

Chapter 3: Heating effect on growth kinetics of nanofibers

3.1 Introduction

In bulk phase, the effect of temperature on structural behavior and transition temperature on SELPs is well studied [21, 33]. The transition temperature is defined as the temperature at which SELP changes from the gel-like phase to the sol phase. That the structure of SELPs can control a single motif that enables control of the transition temperature is one of the reasons that SELP shows promise in many drug delivery applications. This study showed that SELP proteins form a fibrillose structure only on the surface, and that surface coverage is also influenced by pH and ionic strength [25]. However, the effect of temperature on fibril formation has not yet been determined.

3.2 Methods

To investigate the effect of temperature on fiber self-assembly, the commercial AFM temperature-controlling chamber, BioHeater™ (Asylum Research Inc., Santa Barbara, CA), was incorporated into the experiment.

3.2.1 Experimental arrangement

3.2.1.1 SELP-815K sample preparation on the BioHeater™ heating chamber

A 1 µg/ml SELP-815K solution--a lower concentration than that used for force stimulus--was used to lower the nanofiber surface coverage so as to observe a different growth pattern. Each sample was prepared by dispensing 40 µl of SELP

solution on a freshly cleaved 8 mm × 8 mm mica surface (Ted Pella, Inc., Redding, CA) on a circular glass slide. The samples were incubated for 30 minutes in a humidity chamber at room temperature, and then washed three times with distilled water.

The BioHeaterTM was mounted on the AFM stand and the thermometer tip was inserted into the heating stage and screwed tightly; then the chamber was filled with 2 ml of water. Next, the sealing membrane was clamped onto the cantilever holder and the AFM probe mounted. After the scanner was centered, the AFM head was repositioned on the scanner stand. Once the experimental setup was completed, the normal AFM scanning procedure could be followed.

3.2.1.2 SELP-815K AFM imaging in the BioHeaterTM heating chamber

An MLCT probe (Brucker Corp., Camarillo, CA) with a spring constant ranging from 0.03 to 0.06 N/m was used for SELP-815K imaging. A 10 μm × 10 μm area was scanned with the free amplitude of 41 nm. The set-point amplitude was varied from 20 nm to 38 nm, depending on the image quality, but it was maintained below 38 nm to minimize the effects of nanomechanical stimulus. The chamber was heated up to preset temperatures (28, 33, 37, 40 and 45 °C) and the AFM images were obtained at that specific temperature to monitor the nanofiber growth rate. The images were collected at the same site to obtain the growth rate of the individual nanofiber.

3.2.2 Data Analysis

Using the ImageJ plug-in NeuronJ, the AFM images were converted into grey scale. Furthermore, using the trace function, the software can fit the fiber, measure its

length and record the data in a table, which can be exported for analysis into MS Excel or Origin software applications to determine fiber length distribution.

3.3 Results

Figure 15 shows the temperature increasing from 28 to 45 °C. The heating process ramp rate was 1 °C/min and the waiting time for equilibrium was 1 minute.

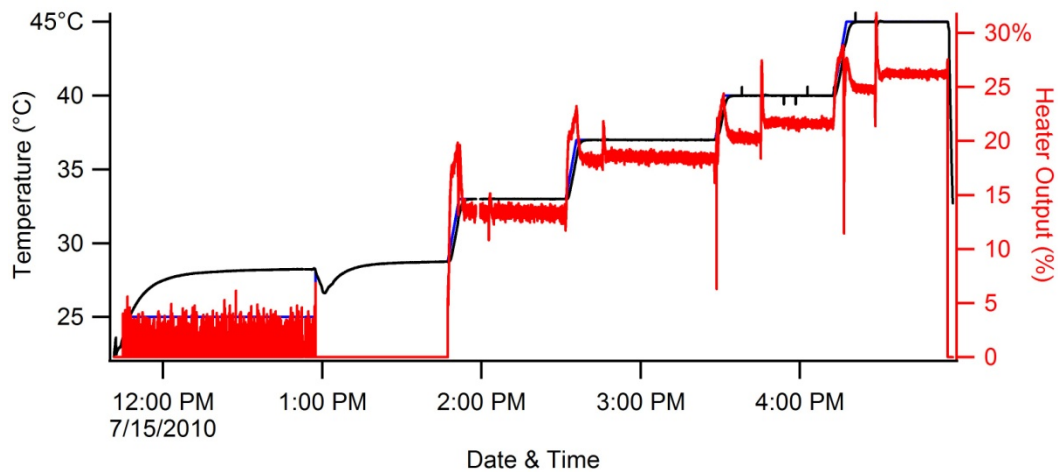


Figure 15. The temperature variation profile during the experiment.

To ensure that the protein was fresh and the force stimulus worked at every temperature level, the scanning process was repeated.

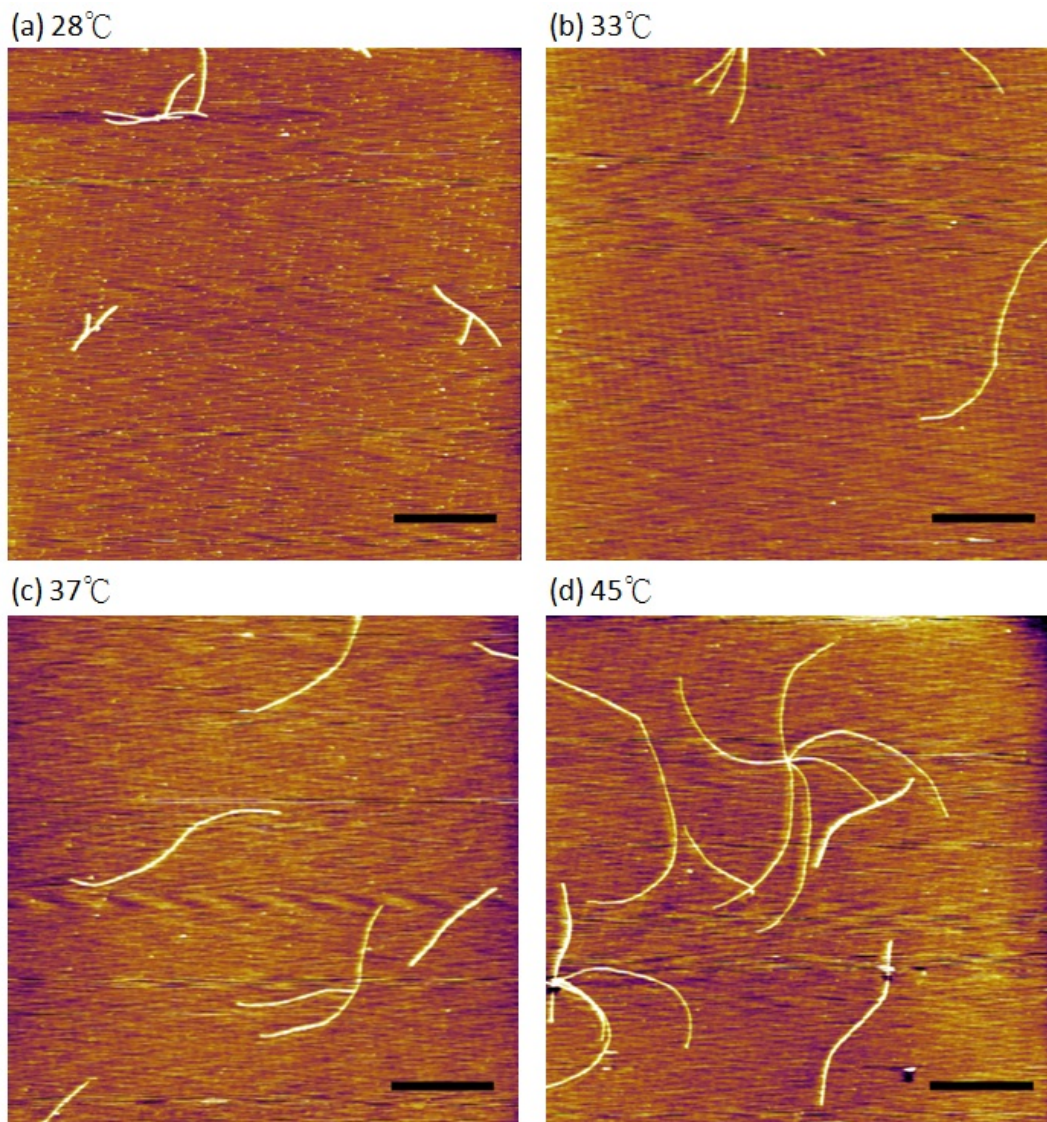


Figure 16. The SELP-815K AFM images under different temperatures. The scale bars correspond to 1 μm .

The qualitative effect of the temperature on nanofiber growth is shown in Figure 16. The information is quantified using NeuronJ to measure the fiber length, given in Figure 17.

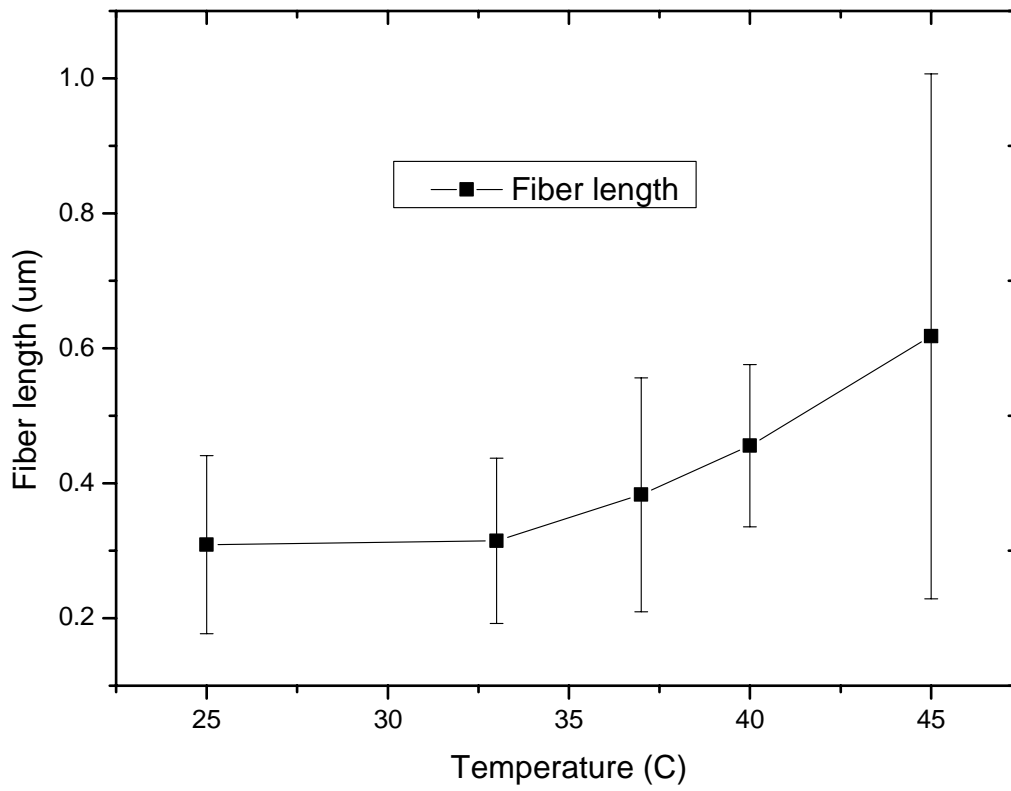


Figure 17. The length of nanofibers measured at different temperatures.

From Figure 17, it can be seen that the fiber growth trend was positively correlated with the temperature. The activation energy was calculated by fitting the curve given by the Arrhenius equation below, where A is the frequency factor for the reaction, R is the universal gas constant, T is the temperature (in °Kelvin), and k is the reaction rate coefficient.

$$k = A \exp\left[\frac{-E_a}{RT}\right]$$

$$\ln k = \frac{-E_a}{RT} + \ln A$$

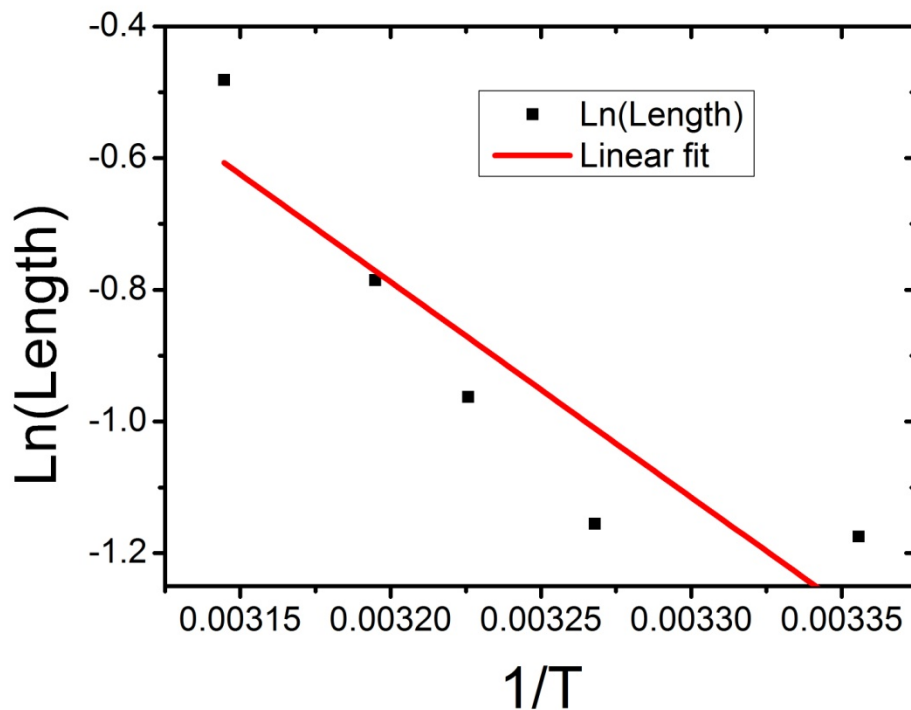


Figure 18. The Arrhenius plot of elongation rates as a function of inverse temperature.

To obtain the activation energy, the line in Figure 18 was fitted using linear least squares in the Origin software application. The fitting equation is shown below.

$$y = -3267.5x + 9.6677$$

$$3267.5 = \frac{E_a}{R}$$

$$\Rightarrow E_a = 27.16 \text{ kJ / mol}$$

Once each term is compared, the activation energy of elongation of ~27 kJ/mol was obtained.

Chapter 4: Discussion

Conformational change and water expulsion

The self-assembly of the nanofiber without a supply from the bulk phase indicates that the concentration of the pre-adsorbed SELP-815K on the mica surface is likely in a supersaturated state. This two-dimensional, densely packed state is formed due to strong coulombic interactions between the negatively charged mica surface and positively charged SELP in distilled water, possibly through the fly-casting mechanism [34]. Once SELPs form a densely packed two-dimensional surface, they hardly self-assemble into nanofibers without mechanical stimulus. The local pressure exerted by the AFM tip during imaging likely lowers the activation energy required for self-assembly, facilitating the rearrangement of the SELP molecules. The activation process may include overcoming strong electrostatic interactions between SELP and mica, conformational changes into a densely packed state, and surface diffusion. This rearrangement process can be further enhanced by water expulsion from the SELP protein under tapping pressure, assisting self-assembly [35]. These molecular level mechanisms can result in increases in both nucleation and elongation rate, as observed in the present system.

Force effect

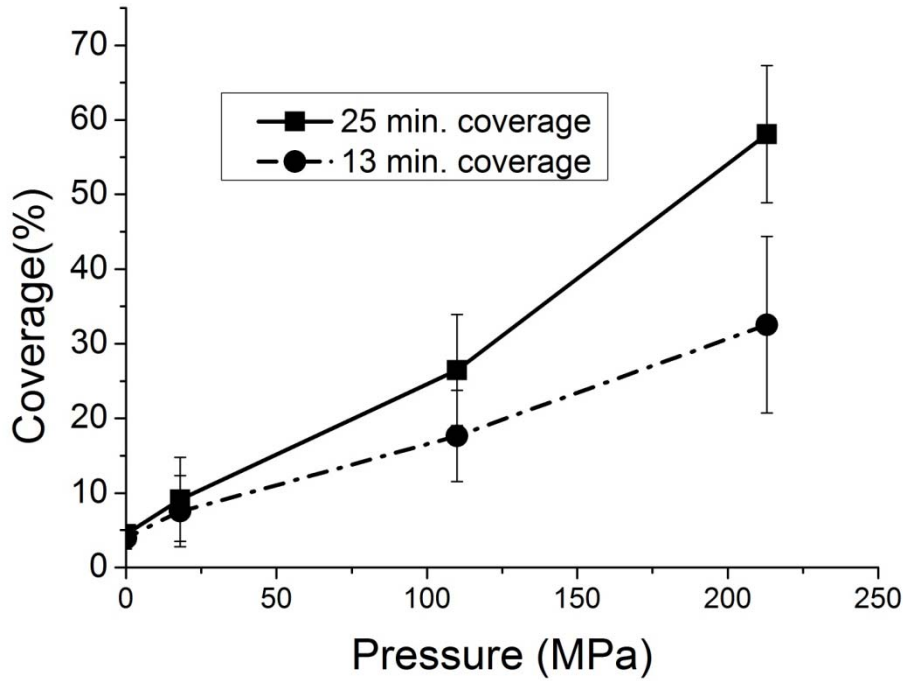


Figure 19. The nanofiber coverage as a function of tapping pressures at different time periods.

In the pressure variation experiment, the fiber growth rate seems linearly proportional to pressure level (Figure 19). This effect could be explained by more kinetic energy being transmitted to the pre-adsorbed protein by a larger tapping force that provided higher energy to the protein to overcome the activation energy required for various molecular level process described previously.

Nanofiber orientation

The newly grown nanofibers had a directional growth pattern after AFM scanning that could have resulted from AFM tip scanning (Figure 20).

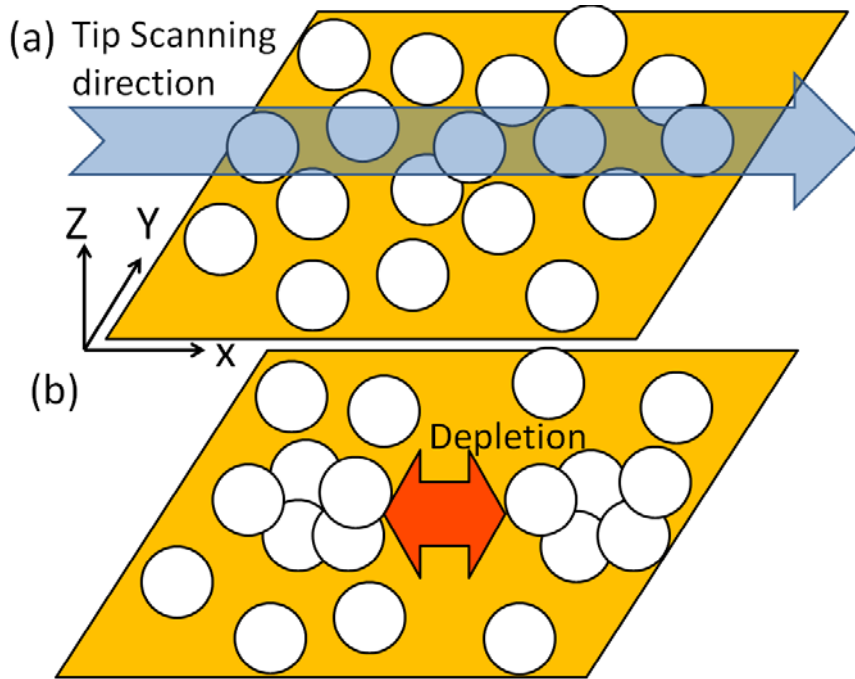


Figure 20. A schematic illustration of fiber growth orientation.

The AFM tip not only provided the normal force (Z -direction) on the surface, but also the horizontal (X -direction) movement because of the scanning pattern. The AFM tip colliding with the pre-adsorbed molecule may have caused the molecule to migrate along the scanning direction, forming nuclei along the scanning direction. In this case, there would be a zone of depleted material between each nucleus (Figure 12c). Due to the limited supply of proteins in the scanning direction, the nanofibers may have more tendency to grow in the Y -direction, which is perpendicular to the scanning direction.

Fiber elongation during heating

In the temperature variation experiments, it was observed that as the temperature increased over time, average fiber length increased. The preformed fibers, the length does not increase as time passes (20 minutes). This elongation phenomenon could not be observed in previous experiments because of the high protein concentration (5ug/ml) used, causing more fiber growth and a faster formation of the network, rather than continuous elongation. It was observed that the fiber stopped growing when it encountered another fiber. Figure 17 shows the average length at different temperatures. This effect could be explained by free energy increase and nanofibers may have an equilibrium length for different temperature settings. As this is an important finding, further studies could focus on collecting more data because there is a large standard deviation at high temperature.

Activation Energy

Using the heating effect data presented in Chapter 3, the value of activation energy of elongation was estimated as ~ 27 kJ/mol, which is close to the amyloid fiber elongation activation energy found in a recent report [36]. According to reports from other studies [37-38], the activation energies of nucleation and elongation for amyloid fiber are shown in Table 4, which is fairly close to the values reported in this thesis.

Table 4. Activation energy on elongation and nucleation for various materials

Material	Ea (Nucleation) kJ/mol	Ea(Elongation) kJ/mol
HET-s[36]	60–71	14–18
Sup35p[37]		11.7 ± 0.2
STVIYE[38]	104.6	

In our system, we applied mechanical stimulus to the sample. This could assist in reconfiguration of the protein and lower both activation energies. Consequently, the protein formed more nuclei and the fiber grew faster on the surface to significantly increase the coverage. We roughly calculated the energy provided when the impact force is ~ 2.9 nN (Table 3) during tapping mode imaging. Assuming the protein size is ~ 4 nm and ~ 4 molecules are compressed under the tip with 5 nm of radius, the energy during the impact is calculated to be 418 kcal/mol ($= (2.9 \text{ nN} \times 4 \text{ nm}) / 4 \text{ SELP molecules} \times 6.02 \times 10^{23} (\text{Avogadro's number}) \times 0.239$ (conversion factor)). This value is higher than the values reported for activation energy for self-assembly in bulk (Table 4) and well above the activation energy based upon our preliminary data. Thus, we confirmed that a few nN impact force during tapping provides enough energy to overcome the measured activation energy, accelerating the nanofiber self-assembly.

Chapter 5: Conclusions

The effect of the mechanical stimulus on nanofiber self-assembly was investigated using silk-elastin like polymers. Chapter 2 demonstrated a novel method to significantly improve and promote the activation of fiber growth on a mica surface by applying different nanomechanical pressure levels to the sample. It also showed that fiber growth is directionally perpendicular to the tip moving trace as the AFM tip contacts the sample. This creates a relatively high density in the vicinity of the scanning area, thus decreasing the energy barrier to form SELP-815K nanofibers. Moreover, simulation of the force level of aqueous scanning was performed to discover the critical force level to initiate growth. These nanomechanical techniques provide a novel way to modify surface properties by pattern peptide self-assembly to produce specific shapes and fiber directions. This technique may be also incorporated in patterning techniques used in tissue engineering and surface modification in biosensors.

The third chapter of this study demonstrated a temperature effect on a protein nanofiber. This technique shows that protein aggregation is highly dependent on the temperature variation, which provides a further understanding of the self-assembly process and protein aggregation. Furthermore, the activation energy that could provide critical information for fiber growth is also calculated, providing a solid foundation for further study of this important process that has applications in both pharmacology and material development.

Appendix I: NanoDrop™ operational procedures

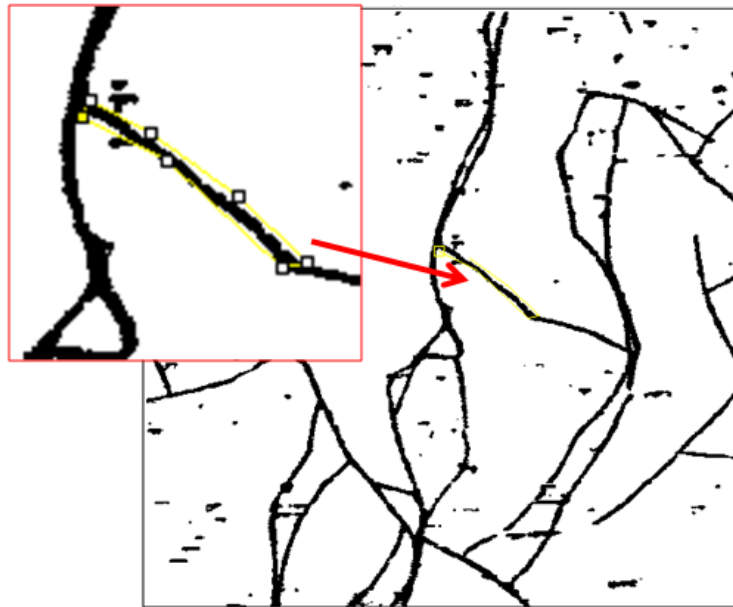
The concentration of the extracted clear solution was measured by NanoDrop (Thermo Fisher Scientific, Wilmington, DE). This procedure involved several steps: first, the application ND-1000 was opened and the protein A280 was selected from a pop-up window. The program prompted for the application of a single water droplet that would calibrate the machine. This was done by dispensing 2 µl of distilled water on the pedestal and closing the arm. The pedestal then automatically adjusted for an optimal path length (0.05 mm – 1 mm). When the measurement was complete, the surfaces were wiped with KIMWIPES® (Kimberly-Clark Worldwide, Inc., Dallas, TX) before proceeding to the next sample. For each subsequent sample, 2 µl PBS was dispensed on the pedestal and “blank measurement” was selected from the available options within the software application. After this sample was analyzed, the pedestal and the arm were wiped clean again, and the SELP-815K solution was deposited on the specimen plate. As in the tests above, the arm was closed, the measurement obtained and the result recorded. The procedure was repeated three times. The arithmetic average was calculated for the results of the three measurements.

Appendix II: Quantification of fiber coverage

At the start of the data analysis procedure, the threshold value output by the software is recorded and the image is exported from the raw AFM file into a tiff image file. The image file is subsequently opened in the ImageJ application and converted to an 8-bit grey scale image. The threshold value is retrieved from MFP-3D to convert the image into a binary file. ImageJ incorporates a function that can measure fiber coverage; thus, the particle circularity should be set to infinity to measure the non-circular objects in the images and the function “measure” should be selected to obtain results. As an output of this procedure, the summary window will show the surface coverage in percentage. The threshold on every image needs to be recorded, together with the corresponding surface coverage.

Appendix III: Quantification of fiber orientation

Similar to the coverage measurement, a grey scale image needs to be produced and the threshold determined to convert it into a binary file, to determinate fiber orientation distribution. Using the polygon selection tool, a polygon is drawn, such that the perimeter outlines a single nanofiber (Figure A1). The “Measure” button on the OrientationJ Measure window is pressed to obtain the measurements, followed by pressing the “Copy Results” button on the same window to obtain all the data that can be pasted into an MS Excel spreadsheet for analysis.



No.	Xc	Yc	Zc	Zone	Ellip...	Prefilter	Energy	Orientation	Coherency
1	1132	890	1	<input checked="" type="checkbox"/>	<input checked="" type="checkbox"/>	0.00	5231.05	-36.75	0.325

Figure A1. An example of measurement of nanofiber orientation.

Glossary of Symbols

A_{actual}	AFM tip actual amplitude
A_{PD}	Photodetector reading amplitude
u	Actual tip position
z_0	Position of the piezo actuator
z_1	First eigenmode cantilever deflection
z_2	Second eigenmode cantilever deflection
m_{eff}	Tip effective mass
k_1	First eigenmode spring constant
k_2	Second eigenmode spring constant
ω_1	First eigenmode oscillation frequency
ω_2	Second eigenmode oscillation frequency
Q_1	First eigenmode quality factor
Q_2	Second eigenmode quality factor
$F_{\text{Deflection}}$	Force applied by the cantilever deflection
$F_{\text{D-cantilever}}$	Liquid damping force on cantilever
$F_{\text{D-Tip}}$	Liquid damping force on tip
H	Hamaker constant
R_{tip}	Tip radius
a_{DMT}	Interatomic distance parameter of a Derjaguin–Müller–Toporov (DMT) potential
E_{tip}	Young's modulus of the tip
ν_{tip}	Poisson coefficient of the tip

E_{sample}	Young's modulus of the sample
ν_{sample}	Poisson coefficient of the sample

Bibliography

1. Kudernac, T., et al., *Two-dimensional supramolecular self-assembly: nanoporous networks on surfaces*. Chemical Society Reviews, 2009. **38**(2): p. 402-421.
2. Jiang, F.Z., et al., *Assembly of collagen into microribbons: effects of pH and electrolytes*. Journal of Structural Biology, 2004. **148**(3): p. 268-278.
3. Huang, Y., et al., *Directed Assembly of One-Dimensional Nanostructures into Functional Networks*. Science, 2001. **291**(5504): p. 630-633.
4. Tans, S.J., A.R.M. Verschueren, and C. Dekker, *Room-temperature transistor based on a single carbon nanotube*. Nature, 1998. **393**(6680): p. 49-52.
5. Cui, Y., et al., *Nanowire Nanosensors for Highly Sensitive and Selective Detection of Biological and Chemical Species*. Science, 2001. **293**(5533): p. 1289-1292.
6. Zhang, J., *Self-assembled nanostructures*. 2003: Springer.
7. Brown, C.L., et al., *Template-directed assembly of a de novo designed protein*. Journal of the American Chemical Society, 2002. **124**(24): p. 6846-6848.
8. Yang, H., et al., *Surface-assisted assembly of an ionic-complementary peptide: Controllable growth of nanofibers*. Journal of the American Chemical Society, 2007. **129**(40): p. 12200-12210.
9. Israelachvili, J.N., *Intermolecular and surface forces : with applications to colloidal and biological systems*. 1985, London ; Orlando, Fla . Academic Press. xv, 296 p.
10. Knowles, T.P., et al., *Role of intermolecular forces in defining material properties of protein nanofibrils*. Science, 2007. **318**(5858): p. 1900-3.
11. Yang, H., et al., *Ionic-Complementary Peptide Matrix for Enzyme Immobilization and Biomolecular Sensing*. Langmuir, 2009. **25**(14): p. 7773-7777.
12. Poole, K., et al., *Molecular-scale topographic cues induce the orientation and directional movement of fibroblasts on two-dimensional collagen surfaces*. Journal of Molecular Biology, 2005. **349**(2): p. 380-386.
13. Cappello, J., et al., *Genetic-Engineering of Structural Protein Polymers*. Biotechnology Progress, 1990. **6**(3): p. 198-202.
14. Megeed, Z., J. Cappello, and H. Ghandehari, *Genetically engineered silk-elastinlike protein polymers for controlled drug delivery*. Advanced Drug Delivery Reviews, 2002. **54**(8): p. 1075-1091.
15. Kaplan, D., *Silk polymers : materials science and biotechnology*. ACS symposium series,. 1994, Washington, DC: American Chemical Society. xi, 370 p.
16. McGrath, K. and D. Kaplan, *Protein-based materials*. Bioengineering of materials. 1997, Boston: Birkhäuser. xx, 429 p.
17. Gustafson, J., et al., *Silk-elastinlike recombinant polymers for gene therapy of head and neck cancer: From molecular definition to controlled gene expression*. Journal of Controlled Release, 2009. **140**(3): p. 256-261.

18. Gosline, J., et al., *Elastic proteins: biological roles and mechanical properties*. Philosophical Transactions of the Royal Society of London Series B-Biological Sciences, 2002. **357**(1418): p. 121-132.
19. Ferrari, F., et al., *Construction of synthetic DNA and its use in large polypeptide synthesis*. 1993, Google Patents.
20. Dandu, R., et al., *Silk-elastinlike protein polymer hydrogels: Influence of monomer sequence on physicochemical properties*. Polymer, 2009. **50**(2): p. 366-374.
21. Nagarsekar, A., et al., *Genetic engineering of stimuli-sensitive silkelastin-like protein block copolymers*. Biomacromolecules, 2003. **4**(3): p. 602-607.
22. Haider, M., et al., *In vitro chondrogenesis of mesenchymal stem cells in recombinant silk-elastinlike hydrogels*. Pharmaceutical Research, 2008. **25**(3): p. 692-699.
23. Lutolf, M.P. and J.A. Hubbell, *Synthetic biomaterials as instructive extracellular microenvironments for morphogenesis in tissue engineering*. Nature Biotechnology, 2005. **23**(1): p. 47-55.
24. Venugopal, J. and S. Ramakrishna, *Biocompatible nanofiber matrices for the engineering of a dermal substitute for skin regeneration*. Tissue Engineering, 2005. **11**(5-6): p. 847-854.
25. Hwang, W., et al., *Surface Induced Nanofiber Growth by Self-Assembly of a Silk-Elastin-like Protein Polymer*. Langmuir, 2009. **25**(21): p. 12682-12686.
26. Garcia, R. and R. Perez, *Dynamic atomic force microscopy methods*. Surface Science Reports, 2002. **47**(6-8): p. 197-301.
27. Herruzo, E.T. and R. Garcia, *Frequency response of an atomic force microscope in liquids and air: Magnetic versus acoustic excitation*. Applied Physics Letters, 2007. **91**(14).
28. Melcher, J., X. Xu, and A. Raman, *Multiple impact regimes in liquid environment dynamic atomic force microscopy*. Applied Physics Letters, 2008. **93**(9).
29. Xu, X., et al., *Compositional Contrast of Biological Materials in Liquids Using the Momentary Excitation of Higher Eigenmodes in Dynamic Atomic Force Microscopy*. Physical Review Letters, 2009. **102**(6).
30. Solares, S.D. and J.C. Crone, *Real-time simulation of isolated biomolecule characterization with frequency and force modulation atomic force microscopy*. Journal of Physical Chemistry C, 2007. **111**(27): p. 10029-10034.
31. Chawla, G. and S.D. Solares, *Single-cantilever dual-frequency-modulation atomic force microscopy*. Measurement Science & Technology, 2009. **20**(1).
32. Solares, S.D. and J.C. Crone, *Real-Time Simulation of Isolated Biomolecule Characterization with Frequency and Force Modulation Atomic Force Microscopy*. The Journal of Physical Chemistry C, 2007. **111**(27): p. 10029-10034.
33. Nagarsekar, A., et al., *Genetic synthesis and characterization of pH- and temperature-sensitive silk-elastinlike protein block copolymers*. Journal of Biomedical Materials Research, 2002. **62**(2): p. 195-203.

34. Levy, Y., J.N. Onuchic, and P.G. Wolynes, *Fly-casting in protein-DNA binding: frustration between protein folding and electrostatics facilitates target recognition*. J Am Chem Soc, 2007. **129**(4): p. 738-9.
35. Levy, Y. and J.N. Onuchic, *Water mediation in protein folding and molecular recognition*. Annu Rev Biophys Biomol Struct, 2006. **35**: p. 389-415.
36. Sabaté, R., et al., *Energy barriers for HET-s prion forming domain amyloid formation*. FEBS Journal, 2009. **276**(18): p. 5053-5064.
37. Scheibel, T., J. Bloom, and S. Lindquist, *The elongation of yeast prion fibers involves separable steps of association and conversion*. Proceedings of the National Academy of Sciences of the United States of America, 2004. **101**(8): p. 2287.
38. Hills Jr, R.D. and C.L. Brooks Iii, *Hydrophobic Cooperativity as a Mechanism for Amyloid Nucleation*. Journal of Molecular Biology, 2007. **368**(3): p. 894-901.